EDGE ARTICLE

Check for updates

Modified chlorophyll pigment at Chl$_{D1}$ tunes photosystem II beyond the red-light limit†

Friederike Allgöwer, [ID] ‡[a] Abhishek Sirohiwal, [ID] ‡[a] Ana P. Gamiz-Hernandez, [ID] ‡[a] Maximilian C. Pöverlein, [ID] [a] Andrea Fantuzzi, [ID] [b] A. William Rutherford [ID] [b] and Ville R. I. Kaila [ID] *[a]

Photosystem II (PSII) is powered by the light-capturing properties of chlorophyll *a* pigments that define the spectral range of oxygenic photosynthesis. Some photosynthetic cyanobacteria can acclimate to growth in longer wavelength light by replacing five chlorophylls with long wavelength pigments in specific locations, including one in the reaction center (RC) (*Science*, 2018, **360**, 1210–1213). However, the exact location and the nature of these long wavelength pigments still remain uncertain. Here we have addressed the color-tuning mechanism of the far-red light PSII (FRL-PSII) by excited state calculations at both the *ab initio* correlated (ADC2) and linear-response time-dependent density functional theory (LR-TDDFT) levels in combination with large-scale hybrid quantum/classical (QM/MM) simulations and atomistic molecular dynamics. We show that substitution of a single chlorophyll pigment (Chl$_{D1}$) at the RC by chlorophyll *d* leads to a spectral shift beyond the far-red light limit, as a result of the protein electrostatic, polarization and electronic coupling effects that reproduce key structural and spectroscopic observations. Pigment substitution at the Chl$_{D1}$ site further results in a low site energy within the RC that could function as a sink for the excitation energy and initiate the primary charge separation reaction, driving the water oxidation. Our findings provide a basis for understanding color-tuning mechanisms and bioenergetic principles of oxygenic photosynthesis at the far-red light limit.

1 Introduction

Photosystem II (PSII) is a light-driven water oxidizing and plastoquinone reducing enzyme that transduces sunlight into chemical energy.[1] The charge separation generates a proton motive force (pmf) across the photosynthetic membranes that drives the synthesis of ATP[2,3] and production of biomass, whilst the release of molecular oxygen powers aerobic life.[4] The photochemistry of PSII occurs in its reaction center (RC), comprising four chlorophyll and two pheophytin pigments, symmetrically embedded in the D1 and D2 subunits (Fig. 1A). The RC pigments comprise a central P_{D1}/P_{D2} chlorophyll pair together with two adjacent chlorophylls (Chl$_{D1}$, Chl$_{D2}$) and two pheophytin pigments (Pheo$_{D1}$, Pheo$_{D2}$) (Fig. 1B).[5,6] This pigment array traps the excitation energy transferred from the light-harvesting antenna and functions as the site for the light-driven charge separation,[6] driving water oxidation at the manganese-oxo-calcium cluster (Mn$_4$O$_5$Ca).

Chlorophyll *a* (Chl *a*) pigments, abundantly present in the photosynthetic proteins, enable efficient light-harvesting of PSII with a maximum absorption around 670 nm (1.85 eV). It has been suggested that the specific Chl *a* involved in PSII photochemistry at 685 nm (1.81 eV) define the "red-limit" of oxygenic photosynthesis, where photons beyond 700 nm (energy <1.77 eV) do not efficiently trigger the charge separation responsible for water oxidation and release of O$_2$. However, the cyanobacterium *Chroococcidiopsis thermalis* acclimatizes to far-red light, by replacing its conventional PSII (white-light PSII; WL-PSII) with a far-red isoform (FRL-PSII), which incorporates one Chl *d* and four Chl *f* pigments instead of Chl *a* into specific locations, while retaining all the other Chl *a* pigments in the antenna and reaction center (Fig. 1A).[7,8] This site-specific 'doping' of the pigments in the FRL-PSII, results in a significant redshift of the absorption spectrum at room temperature with a peak absorption maximum around 715–725 nm (1.71–1.74 eV), partially resolved at cryo-temperatures.[7]

Locating the position and function of these far-red light pigments in PSII is crucial for understanding the mechanistic principles of far-red light driven oxygenic photosynthesis. Nürnberg *et al.*[7] proposed that the far-red chlorophylls were not just acting as an extension to the antenna, but crucially, one of them was serving as the primary donor within the RC. This proposal[7] was based on the efficient far-red light-driven charge

[a]*Department of Biochemistry and Biophysics, Stockholm University, 10691 Stockholm, Sweden. E-mail: ville.kaila@dbb.su.se*

[b]*Department of Life Sciences, Imperial College London, London SW7 2AZ, UK*

† Electronic supplementary information (ESI) available. See DOI: https://doi.org/10.1039/d4sc07473d
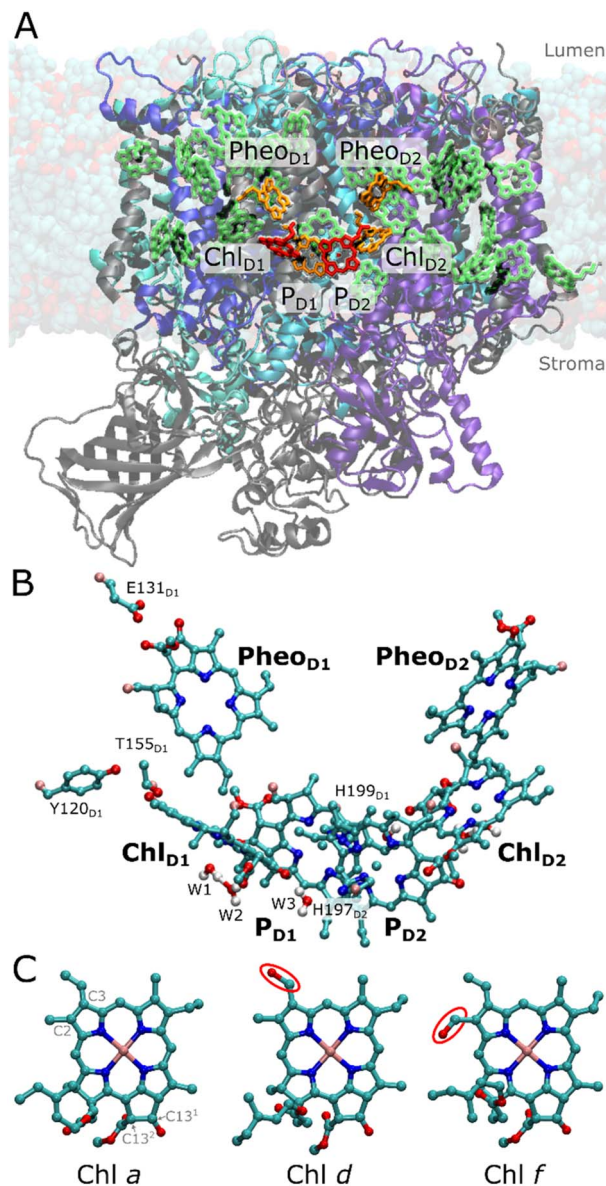
‡ These authors contributed equally.

Fig. 1 Structure of FRL-PSII. (A) Atomistic model of FRL-PSII embedded in a lipid bilayer. The modified protein segments relative to the WL-PSII are shown in blue colors, while unmodified protein is shown in gray. The chlorin-based pigments within the RC are highlighted in orange. Four models of the FRL-PSII were created by modeling Chl d or Chl f at either the Chl_{D1} or P_{D2} site (in red). (B) Closeup of the RC, involving six pigments, hydrogen-bonding residues and nearby water molecules. P_{D1} is axially ligated by D1-His198 in the WL-PSII and D1-His199 in the FRL-PSII, while P_{D2} is axially ligated by D2-His197. Chl_{D1} is axially coordinated by a water molecule (W1), which further interacts through hydrogen-bonding interaction with another water (W2). The figure also shows the W3 water molecule interacting with the C13^1 keto group of Chl_{D1} and the axial histidine ligand of P_{D2}. Chl_{D2} is similarly surrounded by three water molecules. Hydrogen atoms are not shown for clarity. (C) Comparison of the structure of different chlorophyll pigments: Chl a has vinyl group at the C3 position, while Chl d features a formyl group at the C3 position and Chl f a formyl at the C2 position. The differences in structure are highlighted with a red circle.

separation in both room and low temperature, as well as hyperluminescence compared to conventional cyanobacteria PSII. The finding that the Chl d and f pigments not only worked efficiently to absorb lower energy photons, but also acted as the primary electron donor in primary charge separation set both thermodynamic and kinetic boundaries on the chemically challenging photochemistry.[7] Structural factors can be inferred by comparing the chlorophyll binding sites in WL-PSII and FRL-PSII, in particular by the identification of amino acid changes from WL to FRL that introduce new hydrogen-bonding partners for the modified formyl group, leading to a stabilization of the Chl d or f in the binding sites. Despite previous modelling efforts, spectroscopy, and structural studies, the exact location of all the far-red light absorbing pigments remain uncertain.[7–13] For the primary donor, Nürnberg et al.[7] proposed that the Chl_{D1} site was occupied by either a Chl f or the Chl d pigment, while the remaining four Chl f pigments were located in the CP43 and CP47 antennae (cf. ref. 7 for spectroscopic assignment). However, based on the assignment of low-temperature circular dichroism data Judd et al.[9] discussed the possibility that the P_{D2} site could be occupied by Chl f, while accepting that the Chl_{D1} location was also a likely candidate. Ultrafast spectroscopic experiments[10] were interpreted in a model consistent with a far-red pigment at Chl_{D1}, the primary donor, but at that time P_{D2} was not considered as an option. Recent cryo-EM data (PDB ID: 7SA3)[11] suggested a Chl d pigment at the Chl_{D1} site and four Chl f pigments in the integral CP43/CP47 antenna complexes, but these assignments were made at least in part based on the presence of hydrogen-bonding residues close to the putative formal group substitutions, rather than on direct detection of the formyl oxygens, which are structurally difficult to detect[11,14] as the pigments differ only by the chemical substituents on C2 and C3 centers (Fig. 1C).

The changes in the pigments are accompanied by subtle alterations in the pigment binding pockets.[7,8,12] In the FRL-PSII, the D1 core protein has D1-Tyr120 and D1-Thr155 near Chl_{D1}, rather than D1-Phe119 and D1-Ala154 in WL-PSII (Fig. S1 and S2†).[7] The positioning of D1-Tyr120 and D1-Thr155 are thought to facilitate hydrogen-bonding with the formyl group at C3 and C2 of Chl d and Chl f, respectively. In addition, an amino acid substitution was observed near $Pheo_{D1}$, which remains as a Pheo a in FRL-PSII, where the hydrogen-bonding D1-Gln130 in the WL-PSII is replaced by D1-Glu131 in the FRL-PSII. This substitution near $Pheo_{D1}$ is observed as a response to high-light conditions in Chl a-containing PSII (encoded by the psbA3 gene in cyanobacteria T. elongatus and in chloroplast PSII) tuning its reduction potential to higher values.[15,16] However, the mechanisms by which these substitutions could facilitate pigment-binding and spectral tuning remain unclear.

To address the molecular basis of the spectral tuning mechanism to longer wavelengths and its bioenergetic consequences, we perform here large-scale multiscale quantum/classical (QM/MM) simulations and excited state calculations at the correlated ab initio quantum chemical level, using second-order algebraic diagrammatic construction (ADC(2)) theory,[17] as well as linear-response time-dependent density
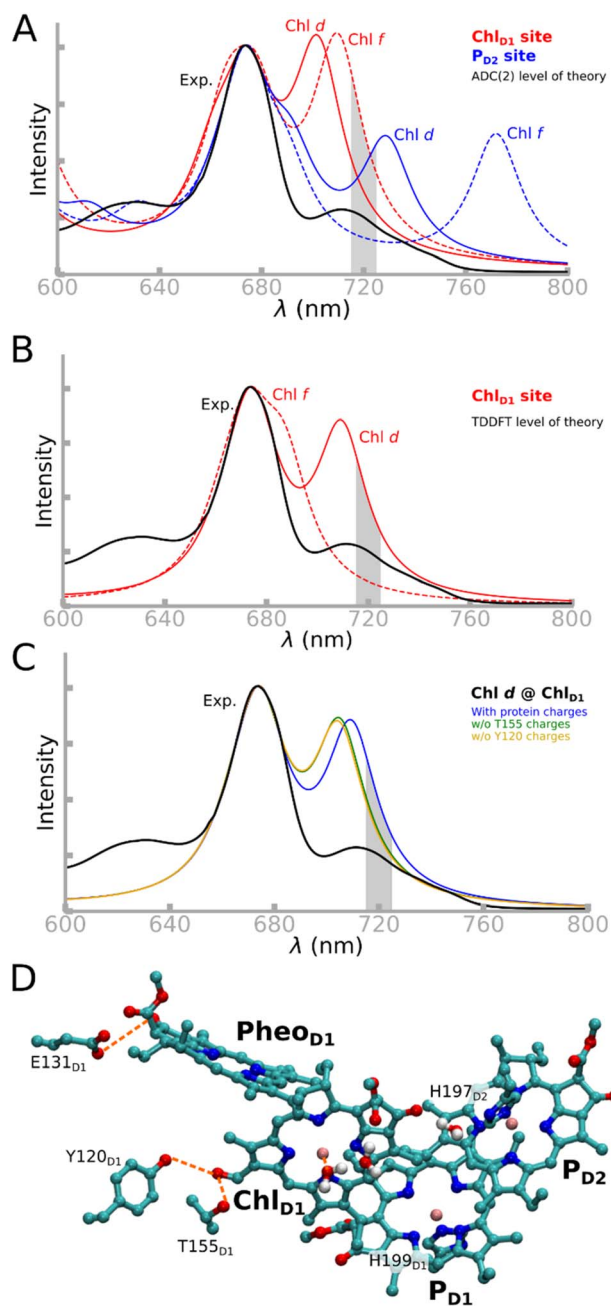
Fig. 2 Absorption spectrum of the FRL-PSII reaction center. (A) Computed absorption spectra based on the tetramer assembly computed at the RVS-LT-SOS-ADC(2)/MM level of theory and comparison with the experimental spectra of the FRL-PSII. The VEEs and the corresponding oscillator strengths were used to compute the spectrum, which was aligned with respect to the 674 nm peak to help the comparison (see ESI, Extended methods†). The FRL region (715–725 nm) is highlighted. Note that the experimental spectra contain the effect of substitutions also beyond the RC (see ref. 7). (B) Computed absorption spectra for substitutions at the Chl_{D1} site at the TDDFT/MM level (ωB97X-V/def2-TZVP, see Methods). The full spectra, including also the substitutions at the P_{D2} site, can be found in Fig. S4A.† (C) Effect of D1-Tyr120 and D1-Thr155 on the absorption spectrum computed at the TDDFT level, and comparison to experimental data. The absorption spectrum shows how selectively removing either D1-Tyr120 and D1-Thr155 blueshifts the far-red transition. (D) Structure of the QM region of the tetrameric pigment model, including the P_{D1}, P_{D2}, Chl_{D1}, $Pheo_{D1}$, and surrounding amino

functional theory (LR-TDDFT). To probe the functional dynamics of the substitutions, we also performed atomistic molecular dynamics simulation (MD) on models of both the FRL-PSII and WL-PSII (see Fig. S3 and Table S1 for computational details†) together with electrostatic calculations to probe redox tuning effects. Our atomistic models allow us to systematically probe the effect of Chl d and Chl f substitutions at distinct positions in the RC, and to derive spectral tuning principles. Our combined findings provide a basis for understanding how the RC traps excitation energy, and triggers charge-separation using the decreased energy available in far-red light.

2 Results

2.1 Probing the effect of long wavelength chlorophylls in the RC

To determine the location and nature of the long wavelength chlorophyll in the FRL-PSII RC, we studied the group of four chlorophylls pigments that are involved in charge separation, *i.e.* P_{D1}, P_{D2}, Chl_{D1}, and $Pheo_{D1}$, using QM/MM calculations with large extended QM regions with up to 600 atoms in the QM region (Fig. 2D, see Methods). First, we calculated the optical spectra when either of the far-red chlorophylls were introduced into the two candidate locations within the RC, *i.e.*, Chl_{D1}, and P_{D2}. We note that while the focus here is on the far-red pigment within the RC, the experimental spectra reflect the properties of all chlorophyll, including the far-red substitutions also in the antenna protein. However, it has been established that the RC chlorophyll absorbs at around 720 nm, as indicated in Fig. 2.[7] We then decomposed the tuning effects into site energies and excitonic coupling effects with their neighboring pigments (see Methods). To this end, we calculated the vertical excitation energies (VEEs) of the RC pigment cluster using QM/MM models of the FRL-PSII and WL-PSII, allowing us to account for the photoexcitation within the pigment cluster at a correlated quantum mechanical level, including the polarizing effect of the complex PSII surroundings (Fig. S3†).

For the first-principles treatment of electron correlation effects, we applied the second-order algebraic diagrammatic construction theory, ADC(2), in combination with systematic virtual space reduction (RVS)[18] and the Laplace transformed (LT) scaled opposite-spin (SOS) treatment.[19–21] The LT-SOS-RVS approximations were carefully benchmarked, revealing a consistent, small shift (<0.1 eV; Table S13†) that was applied to all LT-SOS-RVS-ADC(2) values. All chlorophyll types showed low D_1 diagnostics in the ADC(2) calculations, indicating a single-reference ground state that provides a reliable basis for the excited state calculations (Table S2†). The RVS-LT-SOS-ADC(2) approach allowed us to extend our model to account for the complete reaction center chlorophyll pigment core (6 pigments: 4 chlorophylls and 2 pheophytins) in their protein surroundings, providing a quantitative treatment of electronic excited

acids and water molecules. Hydrogen bonds are shown in dashed orange lines, and hydrogen atoms are omitted for clarity.

states,[22] an approach that has shown promising results for a range of photobiological systems.[21,23–26] All QM/MM models were also treated at the LR-TDDFT level in combination with modern range-separated functionals (*e.g.* ωB97X-V;[27] see Methods, and Table S3†), predicting results highly similar to those from our correlated QM/MM calculations. Our chlorophyll spectra, calculated as an ensemble average over QM/MM molecular dynamics (QM/MM-MD) simulations, reproduce the spectra computed using QM/MM optimized models (Fig. S4E†), thus indicating that our methodology is robust, despite the computationally highly challenging treatment of electronic excited states in extended multi-pigment models. However, as the absorption maxima of the FRL- and WL-PSII differ by only 0.1 eV and are thus within the error limit of the employed methodology, we rely here also on structural and energetic considerations by probing the influence of the environment on the Chl *d* and *f* substitutions with the RC.

At the QM/MM-ADC(2) level (Fig. 2A), when Chl *d* or Chl *f* are modeled at the Chl$_{D1}$ site (with Chl *a* in the other RC pigment locations), we obtain long wavelength transitions at 1.769 eV/701 nm (Chl *d* @ Chl$_{D1}$) and 1.749 eV/709 nm (Chl *f* @ Chl$_{D1}$), respectively. Moreover, when Chl *d* is modeled at the P$_{D2}$ site (Chl *d* @ P$_{D2}$), a prominent absorption feature at 1.703 eV/728 nm is observed, while with Chl *f* at the P$_{D2}$ site (Chl *f* @ P$_{D2}$), an even longer wavelength absorption at 1.606 eV/772 nm arises from the local excitation at P$_{D2}$ (Fig. S5†). Both models with P$_{D2}$ substitutions are strongly redshifted, but the Chl *d* substitution is closer to the experimental absorption at 1.72 eV/720 nm.[7]

In all four FRL-PSII models as well as in the WL-PSII model, a shorter wavelength transition at 674 nm (1.840 eV) can be observed, corresponding to a local excitation at the P$_{D1}$/P$_{D2}$ pair (Fig. S5†). This spectral feature arises both at the ADC(2) and TDDFT level (Fig. 2), suggesting that overall our results are accurate, even when considering the intrinsic error sources of the methods.[22,28]

Conversely, the TDDFT-spectrum of the pigment clusters with Chl *d* at the Chl$_{D1}$ site aligns well with the experimental spectrum for both the far-red band (709 nm/1.749 eV) and the P$_{D1}$/P$_{D2}$ band at 674 nm (1.840 eV), accurately reproducing of the relative intensities of the Q band (Fig. 2B, and Table S4†). Taken together, our findings suggest that Chl *d* at the Chl$_{D1}$ site reproduces key optical features of the FRL-PSII, with further energetic and structural implications (see below).

2.2 The effect of the long-wavelength pigment location on the low-energy spectrum

To break down the individual spectral tuning effects, we calculated site energies (Q$_y$) by estimating VEEs (S$_0$ → S$_1$) of the pigments, first without accounting for the excitonic coupling effect of the surrounding pigments (Table 1), and then subsequently added the coupling effects arising from interactions with surrounding pigments and the protein (see section below; Fig. 3, and Extended methods†).

The Chl$_{D1}$ site shows the lowest Q$_y$ excitation energies when either Chl *d* (1.904 eV) or Chl *f* (1.897 eV) are modeled at the

Table 1 Site energies of the P$_{D1}$/P$_{D2}$ and Chl$_{D1}$ pigments for all PSII models at the RVS-LT-SOS-ADC(2)/def2-TZVP level of theory. An extended list with more pigments can be found in Table S5 (ADC2), and the corresponding TDDFT values in Table S6. All values are reported in units of electron volt (eV)

Location	Chl *d/f* @ Chl$_{D1}$	Chl *d/f* @ P$_{D2}$	WL-PSII
P$_{D1}$/P$_{D2}$	1.936/1.943	1.867/1.786	1.946
Chl$_{D1}$	1.904/1.897	2.007/2.006	1.993

Chl$_{D1}$ site (Table 1). We note that the excitation is localized on the Chl$_{D1}$ (Fig. S6†), supporting that the long wavelength pigment could act as a trap for the excitation energy. The differences between the Q$_y$ energies of Chl$_{D1}$ and P$_{D1}$/P$_{D2}$ are rather small (0.032 eV for Chl *d* @ Chl$_{D1}$, 0.046 eV for Chl *f* @Chl$_{D1}$), suggesting that the exciton could be shared amongst multiple sites (see Table S5†).

For the WL-PSII model, the lowest Q$_y$ excitation comprises the P$_{D1}$/P$_{D2}$ pair together with the Chl$_{D1}$ site. In comparison, the site energy of the Chl *a* pigment at Chl$_{D1}$ in the WL-PSII model (1.993 eV) is at shorter wavelengths, as expected, relative to Chl *d* (1.904 eV) and Chl *f* (1.897 eV). The excitonic couplings between P$_{D1}$ and P$_{D2}$ are significantly larger when Chl *d* (97 cm^{-1}) or Chl *f* (105 cm^{-1}) occupies the Chl$_{D1}$ site, whereas for Chl *a* in the WL-PSII model we obtain an excitonic coupling of 77 cm^{-1} that is slightly lower than the experimental estimates of 80–150 cm^{-1} (see Extended methods, and Table S12†).[29–31]

When Chl *d* or Chl *f* occupy the P$_{D2}$ site, the lowest Q$_y$ excitation energies are predicted at the P$_{D1}$/P$_{D2}$ pair (1.867 eV for Chl *d*, 1.786 eV for Chl *f*; Table 1). Relative to the WL-PSII model (1.946 eV) these Q$_y$ energies are significantly red shifted. The first excited state (S$_1$) of the P$_{D1}$/P$_{D2}$ pair comprises a local excitation on P$_{D2}$ with a small contribution from P$_{D1}$ (Fig. S5†) that can be considered a "delocalized" state, whilst we obtain stronger excitonic coupling of 180–192 cm^{-1} amongst the Chl *a/d* and *a/f* pairs at the P$_{D1}$/P$_{D2}$ site.

Overall, the site energies support that the Chl$_{D1}$ substitutions lead to trapping of the excitation energy at the Chl$_{D1}$ site, similar to what is known about the charge separation process in the WL-PSII, whilst the P$_{D2}$ substitutions could result in trapping of the excitation energy at the P$_{D1}$/P$_{D2}$ site and a non-dominant charge transfer pathway.[32,33] Taken together, the predicted site energies thus support that the Chl$_{D1}$ substitutions lead to a productive charge separation pathway in the FRL-PSII.

2.3 Color tuning of Chl$_{D1}$ site by the protein–pigment interactions

To understand how the protein environment affects the spectral tuning process, we probed the role of protein-induced macrocyclic ring strain and electrostatic effects in addition to the coupling and polarization effects with the surrounding pigments for the Chl$_{D1}$ site (Fig. 3; see Methods). The strain effects were calculated based on the spectral shift of an isolated chlorophyll pigment in the gas phase relative to its protein (QM/MM) geometry. We find that the strain effects have a minor
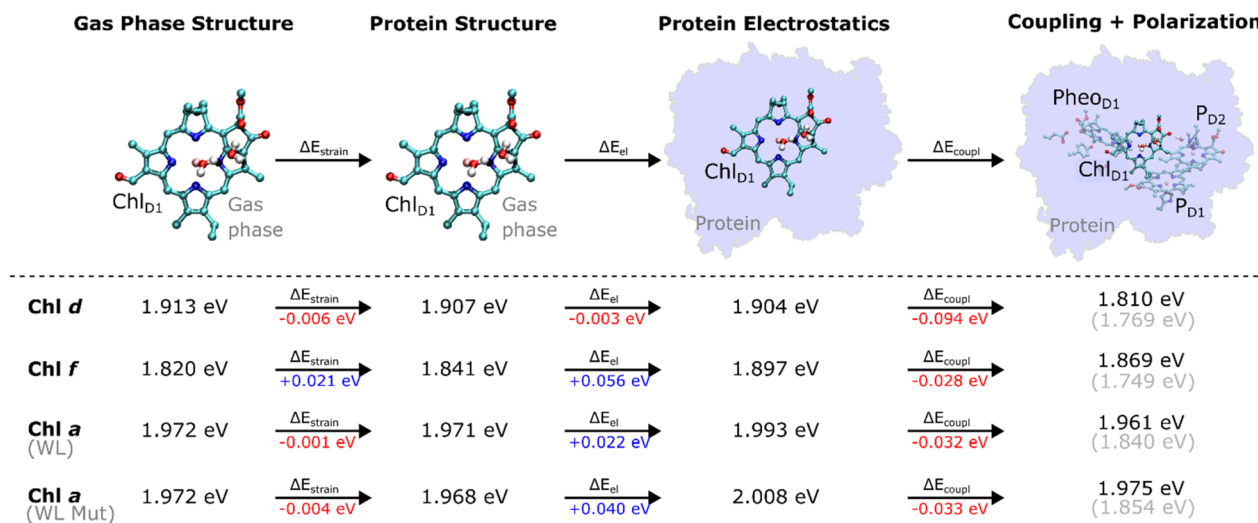
Fig. 3 Probing the spectral tuning mechanism of FRL-PSII. The tuning effect was decomposed into strain, electrostatic, and coupling/polarization for the lowest Q_y excitation for each of the three pigment types at the Chl_{D1} site. Redshifting values are marked in red, while blueshifting values are marked in blue. Electrostatic effects were estimated by computing shifts in VEEs of QM/MM-optimized pigments from the gas-phase to the protein, whilst strain effects were derived from shift of the VEE between the QM/MM-geometry to the gas-phase structure. The grey values in parenthesis refer to the shifted values aligned to the 674 nm peak (see Methods). "WL Mut" refers to the WL-PSII model, with F119Y and A154T mutations. All VEEs are derived from ADC(2) calculations, except the "coupling + polarization" contribution, which was calculated at the TDDFT/ωB97X-V level.

redshifting effect on the VEE of Chl d (−0.006 eV), whereas it has an overall blueshifting effect on Chl f (+0.021 eV) possibly due to the non-preferred binding of the chlorophyll f to the Chl_{D1} site (see below).

Interestingly, the protein electrostatics, including hydrogen-bonding effects, also have a redshifting effect for Chl d (−0.003 eV), but blueshifts Chl f (+0.056 eV) for the Chl_{D1} site, further suggesting that protein electrostatics favors Chl d binding. The differences in electrostatic tuning effects can be attributed to the distinct charge density difference upon the photoexcitation (Fig. S11†) that is favored by the proximity of the C3 formyl group on Chl d to the hydrogen-bonding D1-Tyr120/D1-Thr155 (Fig. S7†), resulting in an overall redshift for Chl d, but no hydrogen-bond and an overall blueshift for Chl f (see also Fig. 2C and S8†). When D1-Tyr120 and D1-Thr155 are modeled into the WL-PSII (replacing D1-Phe119 and D1-Ala154), a blueshift occurs of only 5 nm (0.015 eV) in the Q_y band of the Chl a at the Chl_{D1} site (Fig. 3 and Table S7†).

Excitonic coupling with surrounding pigments and quantum mechanical polarization effects further redshift the excitation energy (0.032 eV) relative to the monomeric pigment for Chl d (Fig. 3). Overall, these findings suggest that the intrinsic light-capturing properties of the Chl d pigment are enhanced relative to Chl f at the Chl_{D1} site by a combination of strain, electrostatics, and coupling/polarization effects, which result in tuning its color and redox properties as the primary electron donor (see below).

2.4 Comparing the functional dynamics of the FRL-PSII and WL-PSII

To explore how the protein dynamics are affected by the FRL substitutions, we studied the FRL-PSII and WL-PSII with Chl d

or Chl f modeled at the Chl_{D1} or P_{D2} sites with atomistic molecular dynamics (MD) simulations (see Table S1† for model constructs and analysis). The MD simulations of FRL-PSII with Chl d at Chl_{D1} reveal a stable hydrogen-bonding interaction between the formyl group (–CHO) of Chl d at the C3 position and both D1-Tyr120 and D1-Thr155 (Fig. 4), which converges at least locally on the simulation timescale (Fig. S17†). In the MD trajectory, the D1-Tyr120-formyl interaction is slightly favored over the D1-Thr155-formyl hydrogen-bond, whilst our QM/MM-MD simulations favor the latter, possibly due to polarization effects (Fig. S10†). In contrast, Chl f does not form similar hydrogen-bonding interactions at the Chl_{D1} site, as the formyl group occupies the more distant C2 position (Fig. 1C and S1C†), both rotamers point away from D1-Tyr120 throughout the simulations. Similarly, we observe no interactions between D1-Tyr120/D1-Thr155 when Chl a, which lacks a formyl group at the C3 position, is modeled at the Chl_{D1} site (see also Fig. 4A–C). In addition to a possible polarization effect, the accuracy of the structural models could affect the relative stability of the hydrogen bonds.

The P_{D2} pigment is stabilized through a hydrogen-bonding interaction to D2-Tyr191 *via* the C13^2 group in the FRL-PSII model (D2-Trp191 in WL-PSII), as well as stacking interactions with P_{D1}. To this end, no hydrogen-bonding interactions are seen between the protein and the formyl groups Chl d or f when they occupy the P_{D2} site (Fig. S10A†). The formyl group of Chl d, when in the P_{D2} location, is highly dynamic in the MD simulation, sampling multiple rotameric states. In contrast, the formyl group of Chl f remains in a single rotameric conformation during the MD simulations (Fig. S10B†).

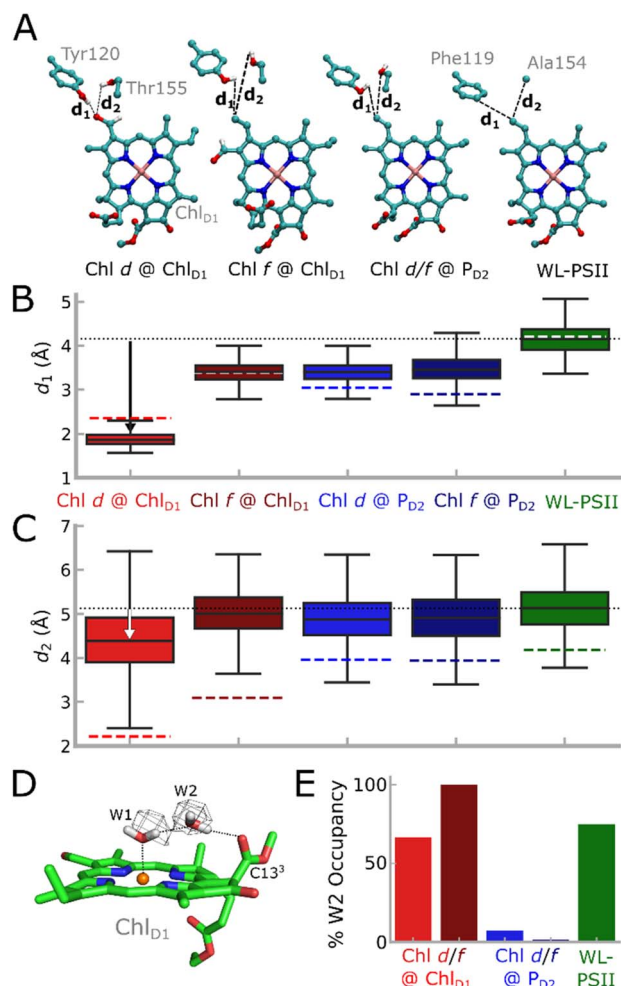In addition to these local interactions, we observe differences in the dynamics of the hydrogen-bonding network around

Fig. 4 Analysis of MD simulations of the FRL-PSII and WL-PSII. (A) Chl_{D1} and its potential hydrogen-bonding partners near the formyl group, namely D1-Tyr120 and D1-Thr155 (D1-Phe119 and D1-Ala154 in the WL-PSII). (B and C) Hydrogen-bonding distance between vinyl (Chl a)/formyl (Chl d/f) group of Chl_{D1} and the (B) D1-Tyr120/D1-Phe119 or (C) D1-Thr155/D1-Ala154 (FRL-PSII/WL-PSII) from the MD simulations. The dotted black line shows the average distance from the WL-PSII MD simulation as a reference. MD distances are shown as a box plot, while QM/MM optimized distances are indicated as colored dashed lines. Boxes indicate the second and third quartiles of the distribution. (D) Water molecules around Chl_{D1}. The water molecule W2 is bound between W1 and the $C13^3$ carbonyl group of Chl_{D1}. The cryo-EM density of the FRL-PSII (PDB ID: 7SA3, EMD-24943)[12] is consistent with the water positions obtained from MD simulations (see also main text). (E) Occupancy of the W2 position in each of the MD models. In the Chl d/f @ P_{D2} simulations W2 escapes the binding pocket.

the Chl_{D1}, especially for a specific water molecule, W2. In the MD simulations W2 forms a hydrogen-bonding link (67% occupancy) between W1, the water that is the axial ligand to Mg^{2+} of Chl_{D1}, and its carbonyl ($C13^2$–$COOCH_3$) substituent (Fig. 4D and E). W2 is structurally conserved at the Chl_{D1} site, and its density is well-resolved in both the WL-PSII and FRL-PSII.[5,12,34] Modifications of the coordinating water molecule and its hydrogen-bonding network can affect both optical and redox properties of the chlorophyll (Table S3 and Fig. S10†).[35–37]

In contrast, for our MD simulations of Chl d and Chl f at the P_{D2} site, W2 near Chl_{D1} escapes from the pigment pocket, possibly due to steric effects, repositioning D2-Leu205 and the propionate group of Chl_{D1} that could affect the local hydration (Fig. 4). These changes are further supported by the smaller sidechain of D1-Leu173 in the FRL-PSII relative to D1-Met172 in the WL-PSII (Fig. S10D†).

Our MD simulations suggest that both Chl d and Chl f at Chl_{D1} lead to subtle structural changes within the RC. We observe a small increase in the P_{D1}/P_{D2} inter-pigment distance (3.65 Å average, edge-to-edge) with Chl d at the Chl_{D1} site relative to the WL-PSII (3.53 Å) (Fig. S10A†) that could influence the electronic coupling (Fig. S13†), charge separation, and electron–hole localization following the charge-separation process. For Chl f at the Chl_{D1} site, the P_{D1}/P_{D2} inter-pigment distance increases to 3.73 Å, most likely due to steric effects.

In contrast, our MD simulations with Chl d and Chl f at P_{D2}, revealed only minor perturbation in the inter-pigment spacing of P_{D1}/P_{D2} (3.55 Å for both Chl a/f and Chl a/d composition). Nevertheless, our calculations suggest that the presence of the long wavelength chlorophyll would affect both the excitonic coupling (Fig. S13†) and redox properties of the pigments (see section below; Table S9†). Although coarse-grained MD simulations have been used to model PSII systems on longer timescales,[38] the atomic detail provided by atomistic MD simulations are central for describing the detailed pigment surroundings.

2.5 Redox tuning and charge transfer kinetics in the FRL-PSII

To probe the binding of the different chlorophylls to the RC, we estimated the binding energies (Fig. S12†) using a PBSA/MM-model based on the MD trajectories (see Extended methods†). Our analysis suggests that Chl d at the Chl_{D1} site has a stronger binding affinity relative to Chl f or Chl a at this position. This effect can be attributed to hydrogen-bonding from D1-Tyr120 or D1-Thr155, stabilizing Chl d relative to the other pigments. For the P_{D2} site, Chl a is better stabilized in comparison to Chl d/f. This likely reflects steric effects from the formyl group, but also the preference for water over histidine as the axial ligand in Chl f, though not in Chl d. Moreover, our binding calculations suggest that the P_{D2} site prefers Chl a.

To probe how the Chl d substitution at the Chl_{D1} site affects the charge separation in the FRL-PSII, we estimated redox potentials based on Poisson–Boltzmann electrostatic calculations coupled with Monte Carlo sampling (PBE/MC), and probed the charge separation kinetics using a kinetic master equation model based on electron transfer theory (see Extended methods†).

Our PBE/MC calculations suggested that the oxidation potential of the Chl_{D1} site increases by 145 mV in the FRL-PSII model with Chl d and by 198 mV with Chl f relative to the WL-PSII model (Fig. S16†). Following the excitation forming the P_{720}^* state at 1.72 eV, the charge separation in the FRL-PSII is thus expected to result in a $Chl_{D1}^+/Pheo_{D1}^-$ state at 1.57 eV with Chl d at the Chl_{D1} site, computed based on the shifts in redox
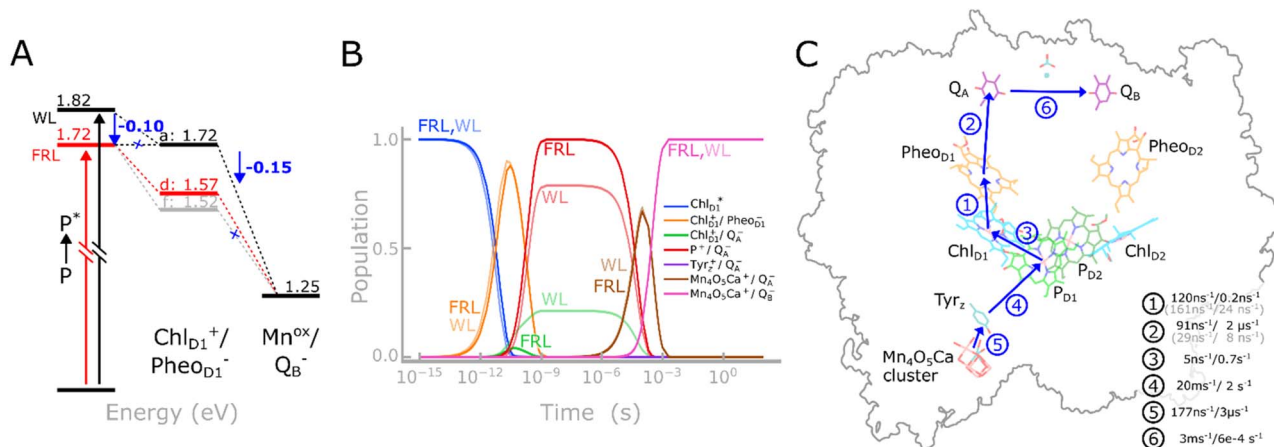
Fig. 5 Probing the charge separation mechanism of FRL-PSII. (A) Effect of the chlorophyll substitution at the Chl_{D1} site on the charge separation energetics based on redox calculations and experimental data. (B) CT kinetics and state populations along the $Chl_{D1}^+Pheo_{D1}^-$-mediated pathway for the FRL-PSII (Chl d @ Chl_{D1}; bright colors) and WL-PSII (transparent colors). (C) Kinetics of charge transfer: light-driven CT at Chl_{D1} leads to a Chl_{D1}^+/$Pheo_{D1}^-$ state, whilst the subsequent electron transfer leads to reduction of Q_B and oxidation of the Mn_4O_5Ca cluster. The arrows indicate the order of events predicted by our kinetic model. The charge transfer rates reported correspond to the FRL system (with Chl d at the Chl_{D1} site), whilst rates that are unique for the WL-PSII model, are shown in grey. See Fig. S15, S16 and Table S10 and ESI, Extended methods for detailed models.†

potentials relative to the WL-PSII. To this end, the PBE/MC calculations suggest that the Chl d modifications at Chl_{D1}, stabilize the charge-separated states due to the hydrogen-bonding effects to surrounding residues by $ca.$ 0.15 eV relative to the WL-PSII system (Fig. 5A), and could thus compensate for the 0.10 eV lower photon energy in the FRL-PSII, while maintaining a significant driving force needed for the water oxidation and quinone reduction.

Interestingly, our PBE/MC models suggest that with Chl f at Chl_{D1}, the $Chl_{D1}^+Pheo^-$ charge separated-state becomes more stabilized possibly due to its intrinsically higher oxidation potential relative to Chl d and a (Fig. 5A and S16†). The shifted redox properties result in less driving force to stabilize the subsequent electron transfer steps and could favor recombination and harmful singlet oxygen production, as it is energetically closer to the Mn^{ox}/Q_B^- state (1.25 eV).

Our kinetic models based on the determined energetics (Fig. 5 and S15†), predict that the $Chl_{D1}^+Pheo^-$-mediated charge separation pathway is fast, with a halftime reaching Q_B reduction/Mn oxidation within $ca.$ 300 μs ($cf.$ ref. 16 and 39), which is rate-limited by the slow $Q_A \rightarrow Q_B$ reaction.[40] The shifted redox properties at Chl_{D1} thus support a charge separation kinetics comparable to that in the WL-PSII, despite the lower photon energy and shifted redox properties.

3 Discussion

Our multiscale calculations and prediction of excitation energies showed that the chemical substitution of the Chl_{D1} site by Chl d provides both a structural and electronic model of the FRL-PSII that is consistent with experimental optical spectra[7] and cryo-EM structural analysis[12] (see also Introduction). At this site, Chl d is orientated appropriately to accept a hydrogen-bond from the far-red specific, conserved residues D1-Tyr120 and

D1-Thr155, that tune the absorption, the redox potentials, and increase its affinity to this site.

When Chl f occupies the Chl_{D1} site, our predictions also showed redshifted features that could be consistent with the experimental spectra. However, Chl f in the Chl_{D1} site is not capable of binding to the far-red specific, conserved hydrogen-bonding residues, and the presence of which resulted in a small blueshift of the Chl f Q_y absorption and a lowered binding constant.

When Chl d and Chl f were modeled at the P_{D2} site, it led to a large redshift of the longest wavelength absorption significantly beyond the experimentally observed range (Fig. 2A and S4A†). Moreover, these models did not show similar structural stabilization as for the chemical substitution at the Chl_{D1} site, as there were no obvious conserved changes in the FRL-PSII that could accommodate, either sterically or by the provision of hydrogen-bonds, the additional formyl groups present on Chl d or f. In addition, the presence of Chl f at the P_{D2} site perturbs the structure of the pigment cluster resulting in the loss of the W2 water that plays a role in the hydrogen-bond network associated with the W1 water that coordinates the Chl_{D1}. Changes in this hydrogen-bonding network can result in spectroscopic and functional changes making the PSII susceptible to photodamage.[36,37] Importantly, the charge transfer kinetics in PSII have been extensivity studied ($cf.$ ref. 6, 16 and 39 and ref. therein). Our kinetic models are consistent with the observed kinetics for the WT-PSII, and reproduce also key observations of the far-red light system (see ref. 13), with redox tuning effects favoring the initial charge separation.

Taken together, our combined findings thus indicate that the *Chroococcidiopsis thermalis* FRL-PSII has a long wavelength chlorophyll at the Chl_{D1} site, with Chl d reproducing key electronic and structural features, and support initial arguments for the Chl_{D1} location for the long wavelength pigments (see

Introduction).[7,9,12] The employed multiscale treatment provides an accurate description of the electronic structure of the pigments, but at a high computational cost. In this regard, recently developed machine learning-based methods [41,42] could provide cost-effective alternatives for the prediction of optical spectra and site energies (*cf.* also ref. 43).

Our excited-state calculations and analysis of transition orbitals (Fig. S6 and S7†) showed that a long wavelength chlorophyll at the Chl_{D1} site gave rise to a low-energy Q_y excitation that could act as the primary donor and result in a $Chl_{D1}^+/Pheo_{D1}^-$ state (Fig. 5A). This primary radical pair state transfers the cation radical (the electron hole) to P_{D1}/P_{D2} pair and transfers the electron to Q_A, creating a transient charge-separated $(P_{D1}P_{D2})^+/Q_A^-$ state, with a $t_{1/2}$ of 0.2 ns (Fig. 5B), as suggested by our kinetic model, and with subsequent electron transfer steps forming $Tyr_z^\bullet(H^+)Q_A^-$ and eventually $Mn^{ox}Q_B^-$ as the final state (Fig. 5C). Interestingly, the chemical substitution of Chl_{D1} compensates for the lower photon energy by the tuned redox properties that could further favor the charge transfer towards the Q_B sites (Fig. 5A). In this regard, recent 2D-electronic spectroscopy (2D-ES) studies of the FRL-PSII[44] found experimental support for a similar $(P_{D1}P_{D2})^+/Chl_{D1}^-$ mediated pathway, although this charge separation was assumed to be initiated from a state in which $Pheo_{D1}$ is pre-reduced. Our kinetic models indicate that Chl a at the Chl_{D1} site (and Chl d/f in P_{D2}) lacks the driving force necessary for initial charge separation in the FRL-PSII, while for Chl f at this site, the $Chl_{D1}^+/Pheo_{D1}^-$ state is energetically further stabilized, and could potentially promote electron back transfer and charge recombination, which in turn leads to the formation of triplet chlorophyll and the production of harmful singlet oxygen. Chl d is unique among the pigments as it supports reasonable charge separation energetics at the Chl_{D1} site, and facilitates fast charge transfer kinetics, which are comparable to the WL-PSII according to our kinetic model. In this regard, our electrostatic calculations, suggest that the charge-separated $Chl_{D1}^+/Pheo_{D1}^-$ pair is stabilized by *ca.* 0.15 eV to compensate for the *ca.* 0.1 eV lower photon energy. Although our current models reveal distinct differences between the FRL- and WL-PSII, elucidating the exact mechanistic details of the charge transfer kinetics will require further detailed structure-based electron transfer calculations.

In contrast, when either Chl d or f occupies the P_{D2} site, our calculations suggest that the excitation energy is likely to be trapped within the RC (Fig. S15, Table S5 and S6†). This retention implies two possible scenarios for functional PSII: either an energetically uphill and kinetically slow energy transfer to Chl_{D1} – the putative site of primary charge separation in the WL-PSII (see above; and ref. 31, 32 and 45–47) – or a direct charge separation event involving P_{D1}/P_{D2}. While modification of the pigment at the P_{D2} site would indeed expand the spectral range of PSII (Fig. 2 and S4†), we speculate that the putative $(P_{D1}P_{D2})^+/Chl_{D1}^-$ state with Chl f at P_{D2} would result in a charge recombination.

Our calculations suggest that the specific FRL-PSII surroundings around Chl_{D1} support the redshifting effect of Chl d that could enhance its intrinsic light-capturing properties at the far-red-light limit, while Chl f at the same position led to blueshifting effects on the intrinsic low-energy Q_y state. We could link these spectral shifts to protein-induced electrostatic and hydrogen-bonding effects, leading to an energetic preference of the Chl d at the Chl_{D1} site. This effect arises specifically *via* the FRL-PSII specific D1-Tyr120 and D1-Thr155 residues that form hydrogen-bonding interactions with Chl d. In summary, considering both the pigment–protein interactions at the Chl_{D1} site, spectral tuning effects, as well as possible bioenergetic advantages in the charge separation process (Fig. 5), our calculations strongly support that Chl d at the Chl_{D1} site enables the FRL-PSII to capture low energy photons beyond the far-red light limit.

4 Conclusions

We have combined here multiscale QM/MM models with atomistic molecular dynamics simulations and excited state calculations to elucidate molecular details underlying far-red light adaptations of photosystem II. Based on our multiscale calculations and analysis of experimental data, we found that modifications of both pigment and protein are critical for enhancing the far-red light absorbing properties of FRL-PSII, which achieves spectral tuning by combined electrostatic and polarization/excitonic coupling effects. Taken together, our work strongly supports the presence of a Chl d pigment at the Chl_{D1} site within the RC, leading to a model yielding low site energies that can initiate the primary charge separation reaction and drive water oxidation. Our study provides a basis for further structure-based assignment of color-tuning mechanisms and bioenergetic principles of oxygenic photosynthesis at the far-red light limit.

5 Materials and methods

Models of the WL-PSII (PDB ID: 3WU2)[5] and FRL-PSII (with Chl $a/d/f$ at P_{D2} or Chl_{D1}) were embedded in a POPC/water/ion simulation box with 100 mM NaCl, and studied using atomistic MD simulations with the CHARMM36m[48] force field together with in-house parameters of the co-factors.[49,50] The MD simulations were propagated for 300 ns in duplicates with a 2 fs integration timestep at $T = 310$ K and $p = 1$ bar using NAMD2.14/NAMD3.[51–53] The trajectories were analyzed with VMD.[54] Optical spectra were computed at the QM/MM level, with 1–6 pigments (100–600 atoms) modeled at the TDDFT or LT-SOS-ADC(2)/def2-TZVP[17,55] level and the MM region at the CHARMM36m level. The QM/MM simulations were performed using the CHARMM/TURBOMOLE interface.[48,56,57] Electronic couplings were calculated using the fragment-excitation difference (FED) approach,[58] as implemented in QChem v. 5.3.[59] Redox properties were estimated by combining quantum chemically computed reduction/oxidation free energies with classical solvation free energies modeled at a linearized Poisson–Boltzmann level, as implemented in APBS.[60] See further details of the multiscale simulations in the ESI, Extended methods.†

Data availability

The data supporting this article, including Extended materials and methods, figures showing ADC(2) and TDDFT spectra, natural transition orbitals, binding free energies, excitonic coupling, site energies, reduction and oxidation potentials, as well as benchmarking calculations, and further computational details can be found in the ESI.† QM/MM-optimized geometries, as well as the homology models are accessible on Zenodo at https://doi.org/10.5281/zenodo.15153234.

Author contributions

V. R. I. K. designed research; F. A., A. S., A. P. G.-H., M. C. P., performed research; F. A., A. S., A. P. G.-H., M. C. P., V. R. I. K. developed analytical tools; F. A., A. S., A. P. G.-H., M. C. P., A. F., A. W. R., V. R. I. K. analyzed data; V. R. I. K., F. A., A. S., A. W. R., wrote the paper with contributions from all co-authors.

Conflicts of interest

There are no conflicts to declare.

Acknowledgements

References

1 R. E. Blankenship, *Molecular Mechanisms of Photosynthesis*, Wiley, 3 edn, 2021.
2 P. Mitchell, *Nature*, 1961, **191**, 144–148.
3 N. Nelson and C. F. Yocum, *Annu. Rev. Plant Biol.*, 2006, **57**, 521–565.
4 V. R. I. Kaila and M. Wikström, *Nat. Rev. Microbiol.*, 2021, **19**, 319–330.
5 Y. Umena, K. Kawakami, J.-R. Shen and N. Kamiya, *Nature*, 2011, **473**, 55–60.
6 T. Cardona, A. Sedoud, N. Cox and A. W. Rutherford, *Biochim. Biophys. Acta Bioenerg.*, 2012, **1817**, 26–43.
7 D. J. Nürnberg, *et al.*, *Science*, 2018, **360**, 1210–1213.
8 V. Mascoli, L. Bersanini and R. Croce, *Nat. Plants*, 2020, **6**, 1044–1053.
9 M. Judd, *et al.*, *Biochim. Biophys. Acta Bioenerg.*, 2020, **1861**, 148248.
10 N. Zamzam, *et al.*, *Proc. Natl. Acad. Sci. U. S. A.*, 2020, **117**, 23158–23164.
11 C. J. Gisriel, J. Wang, G. W. Brudvig and D. A. Bryant, *Commun. Biol.*, 2020, **3**(1), 408.
12 C. J. Gisriel, *et al.*, *J. Biol. Chem.*, 2022, **298**, 101424.
13 S. Viola, *et al.*, *eLife*, 2022, **11**, e79890.
14 J. Wang and P. B. Moore, *Protein Sci.*, 2017, **26**, 122–129.
15 A. W. Rutherford, A. Osyczka and F. Rappaport, *FEBS Lett.*, 2012, **586**, 603–616.
16 M. Sugiura, C. Azami, K. Koyama, A. W. Rutherford, F. Rappaport and A. Boussac, *Biochim. Biophys. Acta Bioenerg.*, 2014, **1837**, 139–148.
17 J. Schirmer, *Phys. Rev. A*, 1982, **26**, 2395–2416.
18 R. Send, V. R. I. Kaila and D. Sundholm, *J. Chem. Phys.*, 2011, **134**, 214114.
19 N. O. Winter and C. Hättig, *J. Chem. Phys.*, 2011, **134**, 184101.
20 Y. Jung, R. C. Lochan, A. D. Dutoi and M. Head-Gordon, *J. Chem. Phys.*, 2004, **121**, 9793–9802.
21 C.-M. Suomivuori, N. O. C. Winter, C. Hättig, D. Sundholm and V. R. I. Kaila, *J. Chem. Theor. Comput.*, 2016, **12**, 2644–2651.
22 A. Dreuw and M. Wormit, *Wiley Interdiscip. Rev.: Comput. Mol. Sci.*, 2015, **5**, 82–95.
23 C.-M. Suomivuori, H. Fliegl, E. B. Starikov, T. S. Balaban, V. R. I. Kaila and D. Sundholm, *Phys. Chem. Chem. Phys.*, 2019, **21**, 6851–6858.
24 C.-M. Suomivuori, A. P. Gamiz-Hernandez, D. Sundholm and V. R. I. Kaila, *Proc. Natl. Acad. Sci. U. S. A.*, 2017, **114**, 7043–7048.
25 A. P. Gamiz-Hernandez and V. R. I. Kaila, *Phys. Chem. Chem. Phys.*, 2016, **18**, 2802–2809.
26 A. P. Gamiz-Hernandez, I. N. Angelova, R. Send, D. Sundholm and V. R. I. Kaila, *Angew Chem. Int. Ed. Engl.*, 2015, **54**, 11564–11566.
27 N. Mardirossian and M. Head-Gordon, *Phys. Chem. Chem. Phys.*, 2014, **16**, 9904.
28 A. Dreuw and M. Head-Gordon, *Chem. Rev.*, 2005, **105**, 4009–4037.
29 G. Raszewski, B. A. Diner, E. Schlodder and T. Renger, *Biophys. J.*, 2008, **95**, 105–119.
30 J. R. Durrant, D. R. Klug, S. L. Kwa, R. Van Grondelle, G. Porter and J. P. Dekker, *Proc. Natl. Acad. Sci. U. S. A.*, 1995, **92**, 4798–4802.
31 F. Müh, M. Plöckinger and T. Renger, *J. Phys. Chem. Lett.*, 2017, **8**, 850–858.
32 A. Sirohiwal, F. Neese and D. A. Pantazis, *J. Am. Chem. Soc.*, 2020, **142**, 18174–18190.
33 M. Capone, A. Sirohiwal, M. Aschi, D. A. Pantazis and I. Daidone, *Angew Chem. Int. Ed. Engl.*, 2023, **62**, e202216276.
34 M. Suga, *et al.*, *Nature*, 2015, **517**, 99–103.
35 B. A. Diner, *et al.*, *Biochemistry*, 2001, **40**, 9265–9281.

36 Y. Takegawa, *et al.*, *Biochim. Biophys. Acta Bioenerg.*, 2019, **1860**, 297–309.

37 M. Sugiura, *et al.*, *Biochim. Biophys. Acta Bioenerg.*, 2024, **1865**, 149013.

38 F. J. van Eerden, T. van den Berg, P. W. J. M. Frederix, D. H. de Jong, X. Periole and S. J. Marrink, *J. Phys. Chem. B*, 2017, **121**, 3237–3249.

39 D. Noy, C. C. Moser and P. L. Dutton, *Biochim. Biophys. Acta Bioenerg.*, 2006, **1757**, 90–105.

40 R. De Wijn and H. J. Van Gorkom, *Biochemistry*, 2001, **40**, 11912–11922.

41 P. O. Dral and M. Barbatti, *Nat. Rev. Chem.*, 2021, **5**, 388–405.

42 E. Cignoni, L. Cupellini and B. Mennucci, *J. Chem. Theory Comput.*, 2023, **19**, 965–977.

43 H. S. Stein, D. Guevarra, P. F. Newhouse, E. Soedarmadji and J. M. Gregoire, *Chem. Sci.*, 2019, **10**, 47–55.

44 Y. Silori, *et al.*, *J. Phys. Chem. Lett.*, 2023, **14**, 10300–10308.

45 G. Raszewski and T. Renger, *J. Am. Chem. Soc.*, 2008, **130**, 4431–4446.

46 H. Tamura, K. Saito and H. Ishikita, *Proc. Natl. Acad. Sci. U. S. A.*, 2020, **117**, 16373–16382.

47 A. R. Holzwarth, M. G. Müller, M. Reus, M. Nowaczyk, J. Sander and M. Rögner, *Proc. Natl. Acad. Sci. U. S. A.*, 2006, **103**, 6895–6900.

48 J. Huang, *et al.*, *Nat. Methods*, 2017, **14**, 71–73.

49 F. Allgöwer, A. P. Gamiz-Hernandez, A. W. Rutherford and V. R. I. Kaila, *J. Am. Chem. Soc.*, 2022, **144**, 7171–7180.

50 A. Fantuzzi, *et al.*, *Proc. Natl. Acad. Sci. U. S. A.*, 2022, **119**, e2116063119.

51 J. C. Phillips, *et al.*, *J. Chem. Phys.*, 2020, **153**, 044130.

52 J. C. Phillips, *et al.*, *J. Comput. Chem.*, 2005, **26**, 1781–1802.

53 F. Allgöwer, M. C. Pöverlein, A. W. Rutherford and V. R. I. Kaila, *Proc. Natl. Acad. Sci. U. S. A.*, 2024, **121**, e2413396121.

54 W. Humphrey, A. Dalke and K. Schulten, *J. Mol. Graph.*, 1996, **14**, 33–38.

55 A. Schäfer, H. Horn and R. Ahlrichs, *J. Chem. Phys.*, 1992, **97**, 2571–2577.

56 S. G. Balasubramani, *et al.*, *J. Chem. Phys.*, 2020, **152**, 184107.

57 S. Riahi and C. N. Rowley, *J. Comput. Chem.*, 2014, **35**, 2076–2086.

58 C.-P. Hsu, Z.-Q. You and H.-C. Chen, *J. Phys. Chem. C*, 2008, **112**, 1204–1212.

59 Y. Shao, *et al.*, *Mol. Phys.*, 2015, **113**, 184–215.

60 N. A. Baker, D. Sept, S. Joseph, M. J. Holst and J. A. McCammon, *Proc. Natl. Acad. Sci. U. S. A.*, 2001, **98**, 10037–10041.